This is a peer-reviewed, accepted author manuscript of the following research article: Azami, A, Khoshanjam, A, Jerez-Mesa, R, Lluma-Fuentes, J & Travieso-Rodriguez, JA 2023, 'A new theoretical model for surface roughness prediction in rotational abrasive finishing process', Wear, vol. 524-525, 204772. https://doi.org/10.1016/j.wear.2023.204772

A new theoretical model for surface roughness prediction in Rotational Abrasive Finishing process

Aref Azami[a,b,*], Ali Khoshanjam[c], Ramon Jerez-Mesa[b], Jordi Lluma-Fuentes[d], Jose Antonito Travieso-Rodriguez [b]

[a] Centre for Precision Manufacturing, DMEM, University of Strathclyde, Glasgow G1 1XJ, UK

[b] Department of Mechanical Engineering, Barcelona East School of Engineering (EEBE), Universitat Politècnica de Catalunya (UPC), Barcelona 08019, Spain

[c] Department of Mechanical Engineering, Tehran Branch, Islamic Azad University, Tehran, Iran

[d] Department of Material Science and Metallurgical Engineering, Barcelona East School of Engineering (EEBE), Universitat Politècnica de Catalunya (UPC), Barcelona 08019, Spain

* Corresponding author: aref.azamigilan@strath.ac.uk

Abstract

Rotational abrasive finishing (RAF) is a new nano-finishing technique in which the finishing forces are applied to the workpiece by the opposite rotations of a stirring-blades and the workpiece. The RAF process allows for finishing the inner and outer surfaces of workpieces, particularly complex ones with axial symmetry. The present study aims to propose a new theoretical model to obtain deeper insights into the material removal mechanism, surface roughness prediction, and forces in RAF process. Since the abrasive-workpiece interaction is random and complex in nature in the RAF, some initial assumptions were considered. To validate the repeatability of the experimental results, the experiments were designed based on the Response surface method (RSM). To validate the new proposed theoretical model, a number of influential parameters were investigated. It was found that the stirring-blade speed (S), working gap (W), and abrasive grain size (A) had significant effects on Ra. The minimum surface roughness (Ra) was obtained to be 46.87 nm at a rotational speed of 600 rpm, a working gap of 1 mm, and grain size of 18 μm. The experimental results were relatively in good agreement with the theoretical results so that the maximum error was about 24%. This can be assumed that the most important explanation for the difference between the theoretical and experimental results can be attributed to the initial theoretical assumptions.

Keywords: Material removal, Surface roughness, Rotational abrasive finishing, nanofinishing

1. Introduction

Today, there is an increasing demand for ultra-precision finishing due to the complex geometries of workpieces in advanced industries and the significant effects of surface roughness on the function and durability of workpieces [1, 2]. Traditional finishing methods, such as grinding and honing, not only have low efficiency in the ultra-precision finishing of complex shapes but also cause surface and subsurface damage to the workpiece. To tackle these shortcomings, researchers have introduced micro/nano-finishing techniques, where free abrasive grains with different mechanisms are employed to more precisely apply and control forces in the process [3, 4].

Researchers have conducted numerous empirical and theoretical studies on such processes to develop new processes and understand the material removal mechanism and surface roughness (Ra). Jain et al. [5] **e**mployed the finite element method (FEM) and classical abrasion theory to model the material removal mechanism and Ra in abrasive flow finishing (AFF). They demonstrated that a rise in the extrusion pressure and percent abrasive concentration raised the material removal rate (MRR) and reduced Ra. Gorana et al. [6] studied the forces applied to an abrasive grain in AFF. They indicated that the rubbing mode was the major factor (compared to the plowing mode) in the deformation mechanism. Gorana et al. [7] conducted a kinematic analysis to investigate the interaction influence of the abrasive grain and workpiece surface. They found that the initial Ra of the workpiece played a key role in AFF. Singh et al. [8] **s**uggested an analytical model to simulate the forces involved in AFF. They incorporated the blunting of the abrasive grain in the process to implement a more realistic simulation. This improved the consistency of the simulation results with experimental data (compared to theoretical results). Fu et al**.** [9] introduced a new model to predict the finished surface profile after AFF, which was similar to the Preston equation. They found that the high pressure and velocity distributions and the turbulent flow field induced by the contraction part of the limited path inlet were the main explanations for the high MRR. Bouland et al. [10] utilized AFF to finish laser powder bed-fused (LPBF)-built workpieces. To investigate the MRR and surface roughness, they conducted numerical simulations and experimental tests on LPBF-built workpieces. The numerical and experimental results were found to be in good agreement. Sankar et al. [11] presented rotational AFF (R-AFF). They applied rotational movement to the workpiece using R-AFF and were able to significantly enhance MRR and the change in the average surface roughness (ΔRa) [12]**.** Singh and Shan [13] developed magnetic AFF (MAFF) and found that a magnetic field near the workpiece in AFF significantly raised the MRR and the ΔRa. Wani et al**.** [14] modeled MAFF to evaluate surface roughness. They found that a magnetic field near the workpiece led to a larger increase in MRR than in surface roughness. Venkatesh et al. [15] modeled ultrasonic-assisted abrasive flow machining (UAAFM). They demonstrated that high-frequency vibration had the largest contribution to the process among other parameters. Barman and Das [16] presented a new tool for magnetic abrasive finishing (MAF) for finishing free-form workpieces. They were able to improve surface roughness by 94%. Misra et al. [17] proposed an analytical model of ultrasonic-assisted magnetic abrasive finishing (UAMAF). They showed that MRR was a function of the initial Ra in UAMAF – i.e., MRR was larger at a higher initial Ra. Kum et al. [18] introduced a new analytical model based on the abrasive properties to examine MRR in magnetic-field abrasive finishing (MFAF). They developed the MRR based on contact mechanics. It was found that the optimal MRR occurred when the abrasive grains were in a close packing condition. Gao et al. [19] modeled MRR based

on the indentation depth of atomized spherical abrasive grains. They demonstrated that MRR increased as the working gap, feed rate, and magnetic abrasive grain size reduced. Zhang et al. [20] introduced a new tool for the magnetic finishing of inner surfaces. They also analyzed the material removal mechanism based on aggressive contact mechanics and Archard abrasion theory, improving surface roughness by 80%. Jha and Jain [21] developed magnetorheological abrasive flow finishing (MRAFF) to finish the inner surfaces of complex workpieces. They indicated that surface finish improvement was directly related to the magnetic field magnitude. Sidpara and Jain [22] measured the normal and tangential forces of single-crystal silicon in magnetorheological fluid-based finishing (MAF). They figure out that the working gap had the largest effect on the process. Ball-end magnetorheological finishing (BEMRF) was developed as a precision polishing technique based on a magnetorheological polishing fluid with rheological properties [23]. It is utilized for the ultra-precision finishing of flat and three-dimensional workpieces [24]**.** Paswan et al. [25] developed magnetorheological honing (MRH) to finish the inner surfaces of cylindrical workpieces. To finish the UHMWPE acetabular cup, Arora and Singh [26] introduced a new semi-spherical tool for magnetorheological finishing (MR). They significantly improved the surface roughness and sphericity of an ultra-high molecular weight polyethylene (UHMWPE) acetabular cup. Ghosh et al. [27] employed MR to achieve nano-roughness on the surface of an oxygen-free high thermal conductivity (OFHC) copper workpiece. Drawing on the finite element method (FEM), an analytical model, and experiments, they proposed the use of a larger working gap, a lower spindle speed, and a lower feed rate for the finishing of the OFHC copper workpiece. Also, Some developments in adavanced abrasive processes are discussed in following. Cao et al. [28] established an analytical model of the wheel wear for the ultrasonic vibration-assisted creep feed deep profile grinding (UVAPG). The experimental results proved that the model was capable of predicting the wear volume in UVAPG with the maximum error of 4.2 %. Miao et al. [29] investigated the surface deformation structures of turbine blade root of single crystal nickel-based superalloy produced under different creep feed grinding conditions. They found that the structure deformation primarily depends on the dislocation slip and the deformation twinning as a supplement. Cao et al. [30] studied the effect of vibration coupling on the L2T1 vibration mode through the theoretical analysis of apparent elastic method and simulation of FEM. They found, compared with Conventional Grinding (CG), the Ultrasonic Vibration-Assisted Grinding (UVAG) had benefits of 15% lower normal grinding force, 11% lower tangential grinding force, 10% lower workpiece surface roughness and fewer defects on the machined surface of Inconel 718 nickel-based superalloy. Cao et al. [31] analyzed the the intermittent cutting behavior in UVG based on material removal probability model. The analytical results of the material removal probability model were in good agreement with the experimental results. Cao et al. [32] developed a novel ultrasonic vibration plate sonotrode for the Ultrasonic Vibration-Assisted Grinding (UVAG). They proved, compared with CG, the normal and tangential grinding forces of UVAG decrease by 35 % and 39 %, respectively.

Rotational abrasive finishing (RAF) is a new finishing technique in which a stirring-blade and the workpiece rotate in opposite orientations to apply the required forces to the workpiece [33]. It enables the precise finishing of inner and outer surfaces, particularly in workpieces with axial symmetry [34, 35]. As RAF is a new finishing process, thus, it is required to further investigate different aspects of RAF. The novelty of this article is to propose a new theoretical model to obtain

deeper insights into surface roughness in RAF. This new theoretical model provides a better ununderstanding of the material removal mechanism, surface roughness prediction, and applied forces for an abrasive grain. To validate the proposed theoretical model, the effects of a number of process parameters on surface roughness were empirically evaluated.

	Nomenclature
A'	Grain-grooved cross-sectional area (mm^2)
A_p	Projected area of indentation (mm^2)
F_{cen}	Centrifugal force (N)
F_f	Finishing force (N)
F_n	Normal force of abrasive grain (N)
F_w	Normal force of workpiece (N)
F_{req}	Resistant force (N)
F_t	Tangential force (N)
H_w	Brinell hardness
L_i	Real contact length (mm)
L_s	Length of stirring-blade (mm)
L_w	Length of the path traveled by the abrasive grain
N_a	Number of abrasive particles simultaneously acting per unit area of contact
N_s	Number of stirring-blade
N_t	Total number of active abrasive grains
P_t	Tangential stress ($^{N}/_{m^2}$)
$\bar{R}$	Distance between the center of the blade to the center of the abrasive particle (mm)
R_a^0	Initial average surface roughness (nm)
R_a^i	Average roughness after the *i*th rotation of stirring-blade (nm)
R_w	Radius of cylindrical workpiece (mm)
V_i	Volume of material removed in rotation *i* of the stirring-blade
V_t	Total volume removed (mm^3)
W_m	Weight removed (mg)
W_s	Width of stirring-blade (mm)
d_a	Diameter of abrasive particle (mm)
d_i	Diameter of indentation (mm)
d_i	Indentation diameter (mm)
m_a	Mass of the abrasive particle
v_a	Rotational speed of Abrasive (rpm)
v_p	Poisson's ratio of particle
v_r	Relative velocity (rpm)
v_s	Rotational speed of stirring-blade (rpm)
v_w	Rotational speed of workpiece (rpm)
ρ_a	Density of abrasive particle ($^{Kg}/_{m^3}$)
ρ_w	Density of workpiece material ($^{Kg}/_{m^3}$)
σ_w	Normal stress of a material (Mpa)

σ_y	Yield strength of the workpiece material (Mpa)
AFF	Abrasive Flow Finishing
BEMRF	Ball End Magnetorheological Finishing
BHN	Brinell Hardness Number
h	Indentation depth (mm)
MAF	Magnetic Abrasive Finishing
MAFF	Magnetic Abrasive Flow Finishing
MAPs	Magnetic Abrasive Particles
MFAF	Magnetic-Field Abrasive Finishing
MRAFF	Magnetorheological abrasive flow finishing
MRF	Magnetorheological Fluid-Based Finishing
MRH	Magnetorheological Honing
MRR	Material Removal Rate
R_a	Average Surface Roughness (nm)
RAF	Rotational Abrasive Finishing
R-AFF	Rotational Abrasive Flow Finishing
SEM	Scanning Electron Microscopy
UAAFM	Ultrasonic- assisted Abrasive Flow Machining
ΔR_a	Change in average surface roughness (nm)
r	Radius of an abrasive particle (μm)

2. Theoretical analysis

In this section, a theoretical model was developed to investigate the material removal mechanism, surface soughness prediction, and the forces involved in the RAF process.

Assumptions:

Figure 1 depicts the different statuses of abrasive grain during the process. Since the abrasive-workpiece interaction is random and complex in nature, therefore, it is difficult and sometimes impossible to accurately simulate the RAF process. Therefore, the proposed model is based on the possible movement of a particle from the stirring blade to the moment it hits the workpiece surface. To simplify the model, some initial assumptions were considered as follows:

- The abrasive grains were spherical and had the same size (diameter).
- Each abrasive grain had an active cutting edge.
- The workpiece surface had a homogenous roughness profile without a statistical distribution (i.e., the same surface roughness).
- The force applied to an abrasive grain and its indentation depth would remain unchanged.

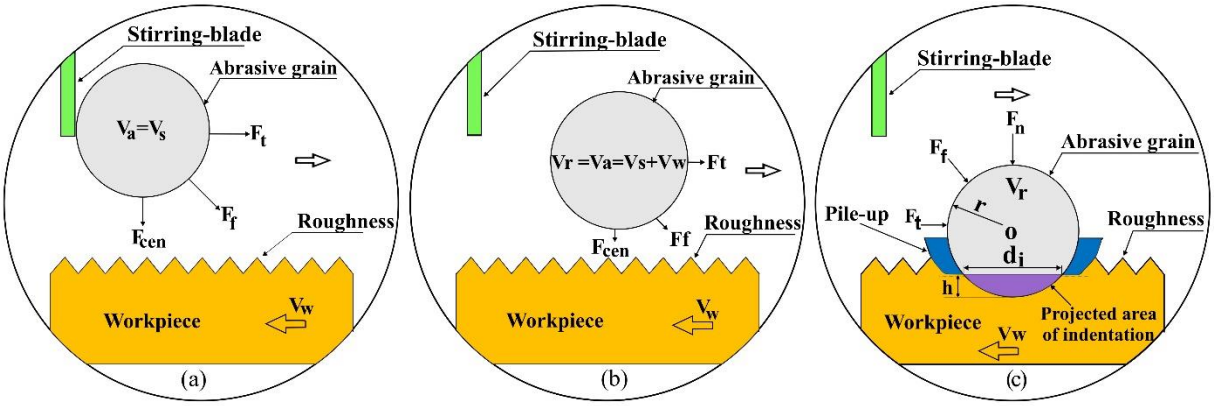

Fig. 1 Stages of the RAF (a) at beginning, (b) before meeting, and (c) during meeting.

2.1. Forces, indentation depth, and abrasive contact area

In RAF process, the relative speed of the stirring-blade and workpiece surrounded by the abrasive provides the force needed to remove material. The movement of abrasive grain on the workpiece surface applies centrifugal (normal) and tangential forces to the workpiece [36]. The centrifugal (normal) force acting on the abrasive grain is responsible to penetrate the workpiece. Then, the abrasive grain moves horizontally on the workpiece surface, leading to micro/nano-scale material removal. The forces involved in the RAF include centrifugal force ($\boldsymbol{F_{cen}}$), normal force ($\boldsymbol{F_n}$), tangential force ($\boldsymbol{F_t}$), and finishing force ($\boldsymbol{F_f}$). The stirring-blade is responsible for rotating the abrasive to penetrate and rub the grains onto the workpiece. Since the stirring-blades and workpiece have no contact and rotate in the opposite directions, they have a relative speed to each other. In the beginning, the abrasive grain speed ($\boldsymbol{v_a}$) is equal to the stirring-blade speed ($\boldsymbol{v_s}$) ($\boldsymbol{v_a = v_s}$). However, due to the relative motion of the stirring-blades and workpiece, the speed of the abrasive grain when meeting the workpiece is equal to the relative speed of the workpiece and stirring-blade ($\boldsymbol{v_r}$) (i.e., $\boldsymbol{v_r = v_a = v_s + v_w}$). The rotation of the stirring-blade induces a centrifugal force in the abrasive. Thus, the indentation force during meeting is equal to the centrifugal force of the abrasive grain. The centrifugal force is defined as:

$$\boldsymbol{F_{cen} = m_a \frac{v_a^2}{\overline{R}}} \quad (1)$$

Where, $\boldsymbol{m_a}$ is the mass of the abrasive particle, $\boldsymbol{v_a}$ is the rotational speed of abrasive grain, and $\boldsymbol{\overline{R}}$ is the distance between the center of the blade to the center of the abrasive grain. Moreover, the mass of an abrasive grain is obtained as:

$$\boldsymbol{m_a = {}^{4}/_{3}\,\pi r^3 \rho_a} \quad (2)$$

Where, $\boldsymbol{r}$ is the radius of an abrasive grain, and $\boldsymbol{\rho_a}$ is the density of abrasive grain.

Therefore, since the speed of the abrasive grain when meeting the workpiece is equal to the relative speed ($\boldsymbol{v_r}$), the centrifugal force ($\boldsymbol{F_{cen}}$) applied to the abrasive grain is obtained by inserting Eq. (2) into Eq. (1) as:

$$\boldsymbol{F_{cen} = {}^{4}/_{3}\,\pi r^3 \rho_a \frac{v_r^2}{\overline{R}}} \quad (3)$$

Where, $\boldsymbol{v_r}$ is the relative velocity. The normal force ($\boldsymbol{F_n}$) acting on an abrasive grain during the meeting is defined as:

$$F_n = F_{cen}\frac{\pi d_a^2}{4} \quad (4)$$

Where, d_a is the diameter of abrasive grain. The insertion of Eq. (3) into Eq. (4) gives:

$$F_n = {}^{4}/_{3}\,\pi r^3 \rho_a \frac{v_r^2}{\overline{R}}\frac{\pi d_a^2}{4} \quad (5)$$

The normal stress (σ_w) of a material is defined by the Brinell hardness (H_w) as [19]:

$$\sigma_w = KH_w \quad (6)$$

According to a report of Jain et al. [36], the coefficient of K is calculated by the type of material (ductile or brittle).

The projected area of indentation (A_p) made by an abrasive grain is expressed as:

$$A_p = \pi\frac{d_i^2}{4} \quad (7)$$

Where, d_i is the indentation diameter of the projected area. Then, the normal force (F_w) applied by workpiece against abrasive grain during the meeting is defined as:

$$F_w = \sigma_w A_p = KH_w\pi\frac{d_i^2}{4} \quad (8)$$

As can be seen in Figure 2(b), the indentation diameter (d_i) and indentation depth (h) can be calculated by the Pythagorean Theorem. The indentation depth is obtained as:

$$h = \frac{d_a}{2} - \frac{1}{2}\sqrt{{d_a}^2 - {d_i}^2} \quad (9)$$

The relation of Brinell Hardness Number (BHN) can be used to obtain the indentation diameter (d_i) in the RAF process, which is defined as follows:

$$BHN = \frac{F_n}{\frac{\pi}{2}d_a\left(d_a - \sqrt{d_a^2 - d_i^2}\right)} \quad (10)$$

By rewriting Eq. (10), the indentation diameter is defined as [25]:

$$d_i = \sqrt{{d_a}^2 - \left(d_a - \frac{2\times 10^{-6}\times F_n}{9.8\pi BHN d_a}\right)^2} \quad (11)$$

Drawing on Eq. (9), the grain-grooved cross-sectional area (A') can be obtained as :

$$A' = \frac{d_a^2}{4}sin^{-1}\left(\frac{2\sqrt{h(d_a-h)}}{d_a}\right) - \sqrt{h(d_a-h)}\left(\frac{d_a}{2}-h\right) \quad (12)$$

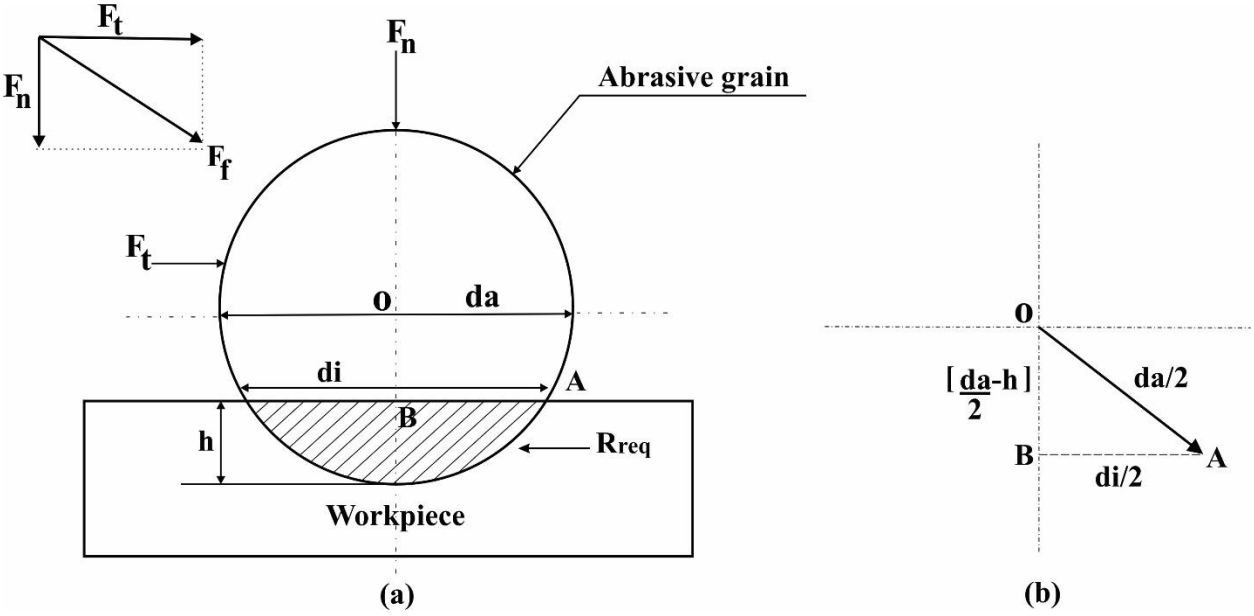

Fig. 2 A schematic of (a) the meeting of an abrasive grain with the workpiece and (b) the OAB triangle induced by abrasive penetration into the workpiece.

Once the abrasive grain has penetrated the workpiece, it moves horizontally on the surface of the workpiece due to the rotational speed of the stirring-blades. The relative speed and thus centrifugal force of the abrasive grain induce tangential stress ($\boldsymbol{P_t}$) to the workpiece. The tangential force ($\boldsymbol{F_t}$) of the abrasive grain, which is responsible for removing material, is defined as [19]:

$$\boldsymbol{F_t = P_t A'} \quad (13)$$

Where,

$$\boldsymbol{P_t = \frac{1 - v_p}{v_p}\, F_n} \quad (14)$$

Where, $\boldsymbol{v_p}$ is the Poisson's ratio of abrasive grain. The insertion of Eqs. (12) and (14) into Eq. (13) gives:

$$\boldsymbol{F_t = \frac{1 - v_p}{v_p}\,\frac{4}{3}\pi r^3 \rho_a \frac{v_r^2}{\bar{R}}\frac{\pi d_a^2}{4} + \frac{d_a^2}{4} sin^{-1}\left(\frac{2\sqrt{h(d_a - h)}}{d_a}\right) - \sqrt{h(d_a - h)}\left(\frac{d_a}{2} - h\right)} \quad (15)$$

Since the workpiece material has a yield strength, the workpiece reacts to the tangential force ($\boldsymbol{F_t}$) and exerts a resisting force ($\boldsymbol{R_{req}}$) in the opposite direction. The resisting force ($\boldsymbol{R_{req}}$) is expressed as:

$$\boldsymbol{R_{req} = \sigma_y A'} \quad (16)$$

Where, $\boldsymbol{\sigma_y}$ is the Yield strength of the workpiece material. Figure 3 illustrates a flow chart of the MATLAB program for material removal occurring. Finishing force ($\boldsymbol{F_f}$) is obtained as the sum of the normal ($\boldsymbol{F_n}$) and tangential forces ($\boldsymbol{F_t}$) as [37]:

$$\boldsymbol{F_f = \sqrt{F_n^2 + F_t^2}} \quad (17)$$

The insertion of Eqs. (5) and (15) into Eq. (17) gives:

$$F_f = \frac{\left(\frac{4}{3}\pi r^3 \rho_a \frac{v^2}{\bar{R}} \frac{\pi d_a^2}{4}\right)^2 + }{\sqrt{\left(\frac{1-v_p}{v_p}\frac{4}{3}\pi r^3 \rho_a \frac{v^2}{\bar{R}} \frac{\pi d_a^2}{4} + \frac{d_a^2}{4} sin^{-1}\left(\frac{2\sqrt{h(d_a-h)}}{d_a}\right) - \sqrt{h(d_a-h)}\left(\frac{d_a}{2}-h\right)\right)^2}} \quad (18)$$

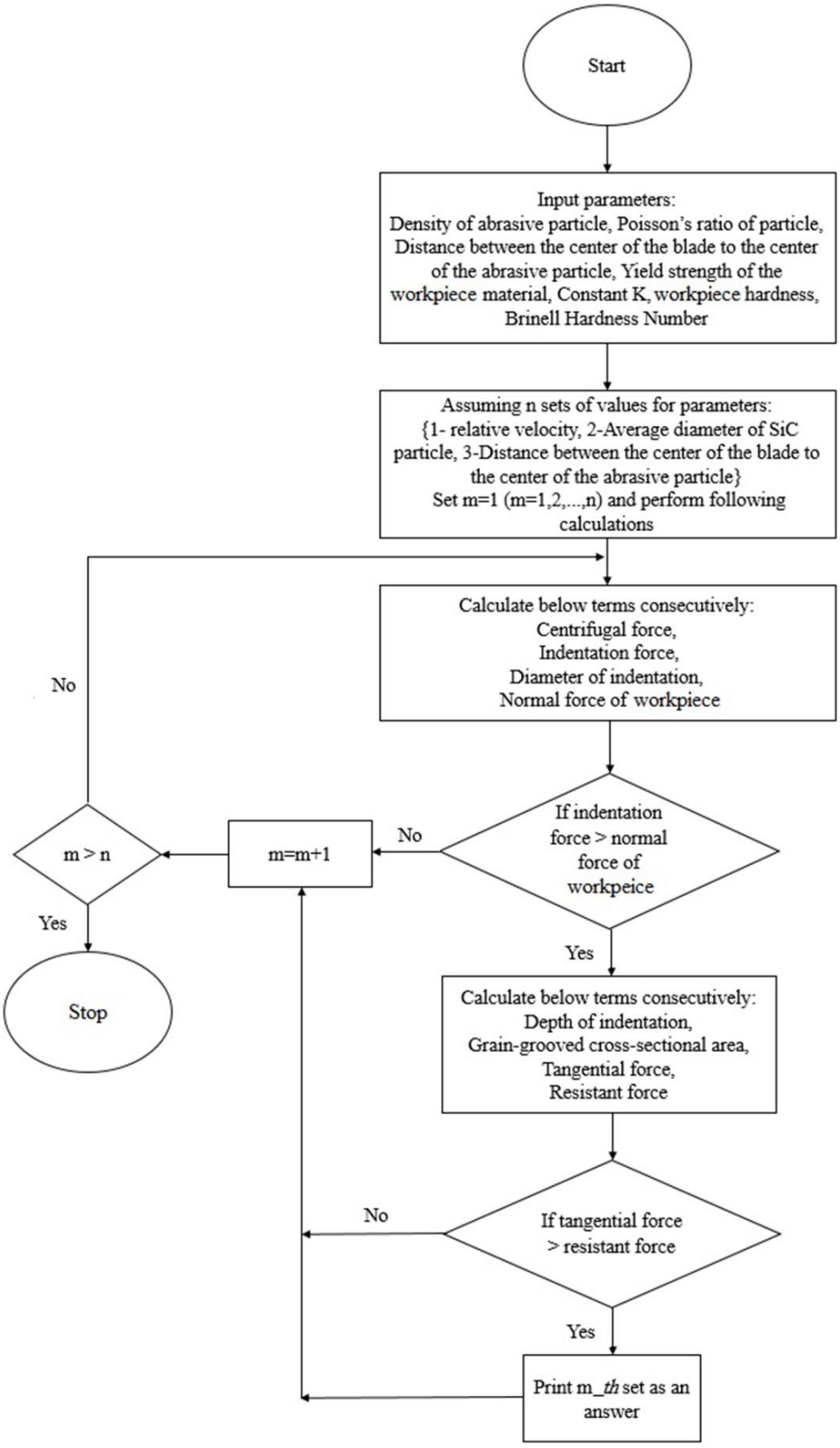
Start
Input parameters:
Density of abrasive particle, Poisson's ratio of particle, Distance between the center of the blade to the center of the abrasive particle, Yield strength of the workpiece material, Constant K, workpiece hardness, Brinell Hardness Number
Assuming n sets of values for parameters:
{1- relative velocity, 2-Average diameter of SiC particle, 3-Distance between the center of the blade to the center of the abrasive particle}
Set m=1 (m=1,2,...,n) and perform following calculations
Calculate below terms consecutively:
Centrifugal force,
Indentation force,
Diameter of indentation,
Normal force of workpiece
If indentation force > normal force of workpeice
No
Yes
m=m+1
m > n
No
Yes
Stop
Calculate below terms consecutively:
Depth of indentation,
Grain-grooved cross-sectional area,
Tangential force,
Resistant force
If tangential force > resistant force
No
Yes
Print m_th set as an answer

Fig. 3 A flow chart obtained from the MATLAB program for material removal mechanism.

2.2. Material removal and surface roughness mechanism

Figure 4 illustrates the contact of the abrasive grain and the workpiece in the working gap. Once the abrasive grain cuts surface roughness, the real contact length ($\boldsymbol{L_i}$) of the grain is calculated as:

$$\boldsymbol{L_i = l_s} \quad (19)$$

Where,

$$\boldsymbol{l_s = 4(R_a^0 - R_a^i)tan\theta_s} \quad (20)$$

Where, $\boldsymbol{R_a^0}$ is the initial surface roughness, and $\boldsymbol{R_a^i}$ is the value of the average roughness after the *i*th rotation of stirring-blades. The length of the path traveled ($\boldsymbol{L_w}$) by the abrasive grain is defined as:

$$\boldsymbol{L_w = l_s + l_g} \quad (21)$$

Where,

$$\boldsymbol{l_s + l_g = 4R_a^0 tan\theta_s} \quad (22)$$

The real contact length ($\boldsymbol{L_i}$) and travel path ($\boldsymbol{L_w}$) are related as:

$$\boldsymbol{L_i = \left(\frac{l_s}{l_s + l_g}\right) L_w} \quad (23)$$

The insertion of Eqs. (20) and (22) into Eq. (23) gives:

$$\boldsymbol{L_i = \left(\frac{4(R_a^0 - R_a^i)tan\theta_s}{4R_a^0 tan\theta_s}\right) L_w} \quad (24)$$

Eq. (24) is simplified into:

$$\boldsymbol{L_i = \left(1 - \frac{R_a^i}{R_a^0}\right) L_w} \quad (25)$$

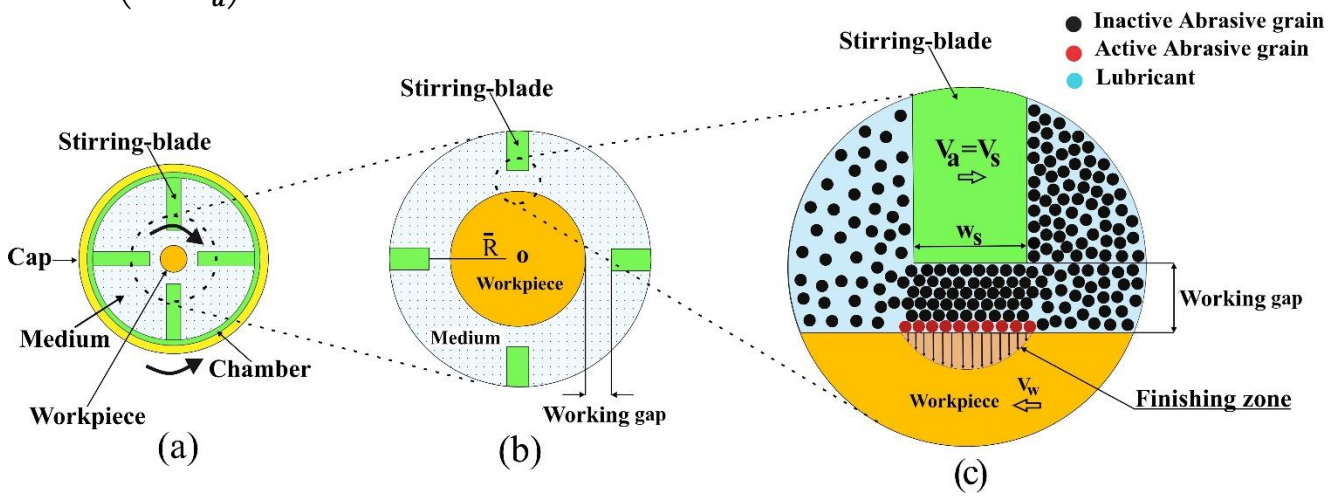

Fig. 4 Schematic of (a) upper view of the stirring-chamber, (b) magnified view of the stirring-chamber, and (c) contact area of the abrasive grain and workpiece in the working gap.

Figure 5 depicts a schematic of Ra. The removal of material is performed by the movement of the abrasive gain on the workpiece once the finishing force exceeds the resisting force. The removed volume is the product of the penetrated area ($\boldsymbol{A'}$) and contact length ($\boldsymbol{L_i}$):

$$V_a = A' L_i \quad (26)$$

The insertion of Eqs. (12) and (25) into Eq. (26) gives:

$$V_a = \left[\frac{d_a^2}{4} sin^{-1}\left(\frac{2\sqrt{h(d_a-h)}}{d_a}\right) - \sqrt{h(d_a-h)}\left(\frac{d_a}{2}-h\right)\right] \times \left(1-\frac{R_a^i}{R_a^0}\right) L_w \quad (27)$$

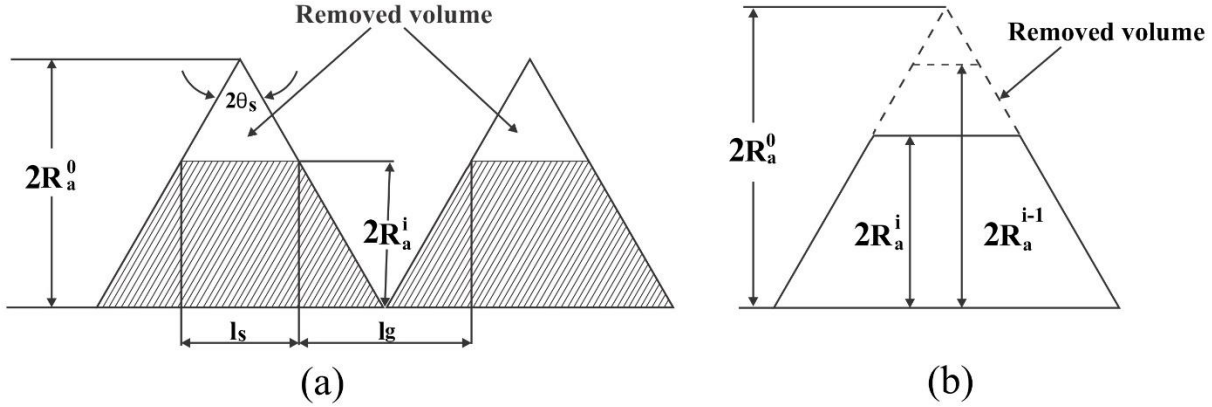

Fig. 5 Schematic of (a) surface roughness and (b) cut peaks after finishing stages.

Material is removed when a large number of abrasive grains move on the workpiece surface. The abrasive grains that participate in the removal of material are known as active abrasive grains (N_a), whereas those that are not involved in the removal process are referred to as inactive grains. The total number of active abrasive grains (N_t) in each stirring-blade rotation is calculated as:

$$N_t = 2\pi R_w N_a N_s W_s L_s \frac{R_s^2}{R_w^2} \quad (28)$$

Where, N_a is the number of abrasive grains simultaneously acting per unit area of contact, N_s is the number of stirring-blade, W_s is the width of stirring-blade, L_s: the length of stirring-blade, R_s is the radius of stirring-blade, and R_w is the radius of cylindrical workpiece.

Therefore, the volume of material removed in rotation *i* of the stirring-blade is obtained as:

$$V_i = A' L_i N_t \quad (29)$$

The insertion of Eqs. (12), (25), and (28) into Eq. (29) gives:

$$V_i = \left[\frac{d_a^2}{4} sin^{-1}\left(\frac{2\sqrt{h(d_a-h)}}{d_a}\right) - \sqrt{h(d_a-h)}\left(\frac{d_a}{2}-h\right)\right] \times \left(1-\frac{R_a^i}{R_a^0}\right) L_w 2\pi R_w N_a N_s W_s L_s \frac{R_s^2}{R_w^2} \quad (30)$$

The total volume removed (V_t) in *n* rotations of the stirring-blade is calculated as:

$$V_t = \left[\frac{d_a^2}{4} sin^{-1}\left(\frac{2\sqrt{h(d_a-h)}}{d_a}\right) - \sqrt{h(d_a-h)}\left(\frac{d_a}{2}-h\right)\right] \times \sum_{1}^{2n}\left(1-\frac{R_a^i}{R_a^0}\right) L_w 2\pi R_w N_a N_s W_s L_s \frac{R_s^2}{R_w^2} \quad (31)$$

Where, $\boldsymbol{\rho_w}$ is the density of workpiece material. Likewise, the total weight removed ($\boldsymbol{W_m}$) in *n* rotations of the stirring-blade is derived as:

$$\boldsymbol{W_m = \left[\frac{d_a^2}{4} sin^{-1}\left(\frac{2\sqrt{h(d_a-h)}}{d_a}\right) - \sqrt{h(d_a-h)}\left(\frac{d_a}{2}-h\right)\right] \times \sum_{1}^{2n}\left(1-\frac{R_a^i}{R_a^0}\right) L_w \rho_w 2\pi R_w N_a N_s W_s L_s \frac{R_s^2}{R_w^2}} \quad (32)$$

The removed volume in stirring-blade rotation *i* can be expressed as:

The removed volume in rotation i = real abrasive contact length × workpiece width × depth of removal.

$$\boldsymbol{V_i = \left(1-\frac{R_a^i}{R_a^0}\right) L_w 2\pi R_w (R_a^{i-1} - R_a^i)} \quad (33)$$

By simplifying Eqs. (30) and (33), surface roughness at the end of iteration *i* and that in iteration *i*-1 are related as:

$$\boldsymbol{R_a^i = R_a^{i-1} - N_a N_s W_s L_s \left(\frac{R_s^2}{R_w^2}\right)\left[\frac{d_a^2}{4} sin^{-1}\left(\frac{2\sqrt{h(d_a-h)}}{d_a}\right) - \sqrt{h(d_a-h)}\left(\frac{d_a}{2}-h\right)\right]} \quad (34)$$

Through the evaluated finishing forces as input parameters, the removal of material in RAF is theoretically calculated. Table 1 represents the constants used in the theoretical analysis. Figure 6 depicts the interaction between the abrasive grain and Ra.

Table 1 Input constant parameters Used during theoretical analysis.

Parameters	**Value**
$\boldsymbol{\nu_p}$	0.14
$\boldsymbol{\sigma_y}$	170 (Mpa)
$\boldsymbol{\rho_w}$	8000 $(^{Kg}/_{m^3})$
$\boldsymbol{\rho_a}$	3220 $(^{Kg}/_{m^3})$
$\boldsymbol{R_w}$	5 (mm)
$\boldsymbol{W_s}$	1 (mm)
$\boldsymbol{L_s}$	10 (mm)
BHN	217

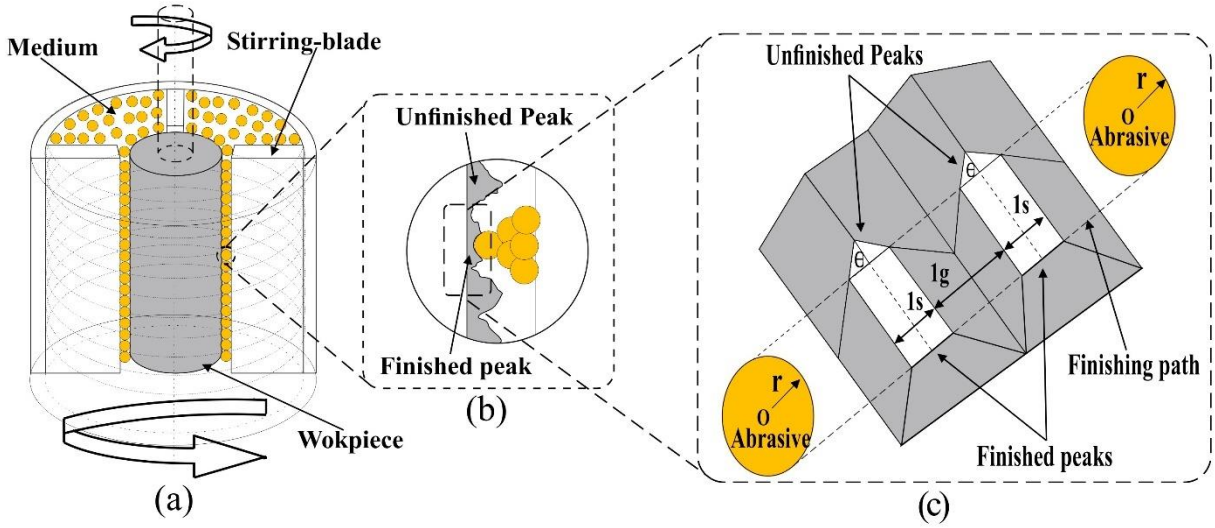

Fig. 6 Interaction between the abrasive and surface roughness.

4. Experimental verification

4.1. RAF set-up

Figure 7 depicts the RAF set-up. The RAF mechanism is based on the simultaneous rotations of the stirring-blades and workpiece in the opposite orientations. To finish the inner surface of the workpiece, the stirring-blade is placed within the workpiece. The stirring-blade is responsible for rotating abrasive grains. There is no contact between the stirring blades and the workpiece surface. The space between the blades and workpiece is known as the working gap in which abrasive is used. The workpiece is placed within a fixture on the bottom of the table connected to the lower electric motor of the set-up. The lower part of the workpiece is sealed using a cap before placing the workpiece within the fixture. Then, the abrasive is poured into the workpiece. The stirring-blade is placed into the workpiece by a fixture on top of the table connected to the upper electric motor of the set-up. Once the stirring-blade has been situated inside the workpiece, another cap is used to seal the top surface of the workpiece. The caps not only prevent abrasive outflow during the process but also provide a closed machining medium, increasing the surface forces, accelerating the process, and reducing the time and cost of the process. The process begins with the stirring-blade rotating the abrasive. The rotation of the abrasive and its contact with the workpiece, which is rotating in the opposite orientations at the same time, provide the required forces of material removal and finishing. Table 2 shows the parameters and experimental setup.

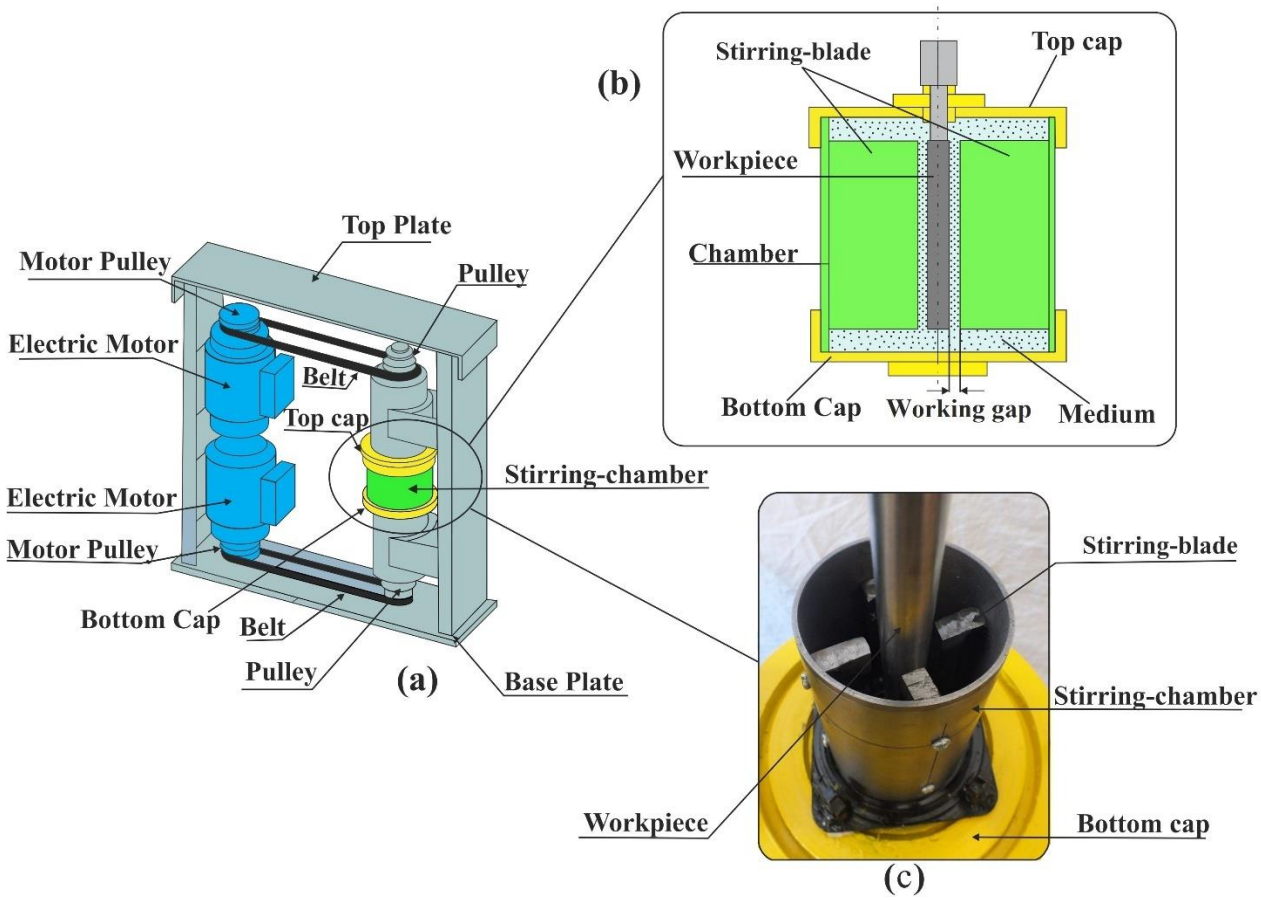

Fig. 7 Schematic of (a) RAF set-up and (b) magnified view and (c) photograph of the stirring chamber and workpiece assembly.

Table 2 Parameters and conditions of experiments.

Name of Parameters	Value
Velocity of stirring-blades (rpm)	300 – 450 – 600
Velocity of workpiece (rpm)	100
Working gap (mm)	1 – 1.5 -2
Workpiece material	Stainless steel 316 L
Abrasive type	Silicon carbide (SiC)
Lubricant type	Naphthenic oil
Weight ratio of medium (SiC : Naphthenic oil)	(70:30)

4.2. Workpiece and abrasive

The present study employed a 316L stainless steel cylindrical workpiece. To obtain the initial Ra of the workpiece, the roughness was measured in random locations, and the average roughness was found to be 303 nm. Also, SiC was employed as the abrasive with an elasticity modulus of 410 GPa and Poisson's ratio of 0.14 [38]. Naphthenic oil was employed as the coolant and the whole process was divided into 5-min cycles. The present study employed abrasive grains with sizes of 18, 23, and 28 μm. Figure 8 shows the SEM images of abrasive grains.

4.3. Material removal and surface roughness measurements

The roughness was measured using a MarSurf PS1 tester with a cutoff or sampling length of 0.25 mm and an evaluation length of 1.25 mm, according to the DIN EN ISO 4288:1996 standard [39]. Surface roughness was measured using the MarSurf PS1 tester at the beginning and end of each experiment. The material removal (MR) was determined experimentally by measuring the weight of workpiece before and after RAF process using electronic balance with an accuracy of 0.001 g [40]. To further examine and compare the results, scanning electron microscopy (SEM) was employed.

4.4. Design of experiments

The design of experiment method (DOE) was used to plan the initial experiments. Initially, Full factorial design was used to plan 18 experiments, as shown in Table 3. Then, the results were exploited to simulate and optimize the influential parameters using the Response surface method (RSM). Table 4 shows the plan of experiments based on the RSM. Accordingly, the rotational speed of the stirring-blade, working gap, and abrasive grain size were investigated as the influential parameters on material removal and surface roughness. In order to verify the repeatability of experiments, a plan of experiment based on the RSM with 3 factors, 2 replication, 20 base runs, and 40 total runs was designed, as shown in Table 4. Accordingly, the final experimental results obtained from the RSM were used to compare with the theoretical results. Surface roughness (Ra) was measured as a function of rotational speed of the stirring-blade (S), working gap (W), and abrasive grain siz (A). Equation (35) shows a quadratic model of the Ra which has R^2 value of 95.70% with the experimental data:

$$Ra = 457 + 0.221\,S + 404.1\,W - 61.17\,M - 0.000698\,S*S - 77.8\,W*W + 1.472\,M*M - 0.0817\,S*W + 0.01117\,S*M - 2.80\,W*M \quad (35)$$

Table 3 Plan of experiments based on the Full factorial method.

StdOrder	RunOrder	PtType	Blocks	S (rpm)	W (mm)	A (μm)
16	1	1	1	600	1.5	28
5	2	1	1	300	2.0	18
3	3	1	1	300	1.5	18
9	4	1	1	450	1.5	18
1	5	1	1	300	1.0	18
13	6	1	1	600	1.0	18
17	7	1	1	600	2.0	18
14	8	1	1	600	1.0	28
12	9	1	1	450	2.0	28
18	10	1	1	600	2.0	28
8	11	1	1	450	1.0	28
6	12	1	1	300	2.0	28
15	13	1	1	600	1.5	18
11	14	1	1	450	2.0	18
7	15	1	1	450	1.0	18
10	16	1	1	450	1.5	28

2	17	1	1	300	1.0	28
4	18	1	1	300	1.5	28

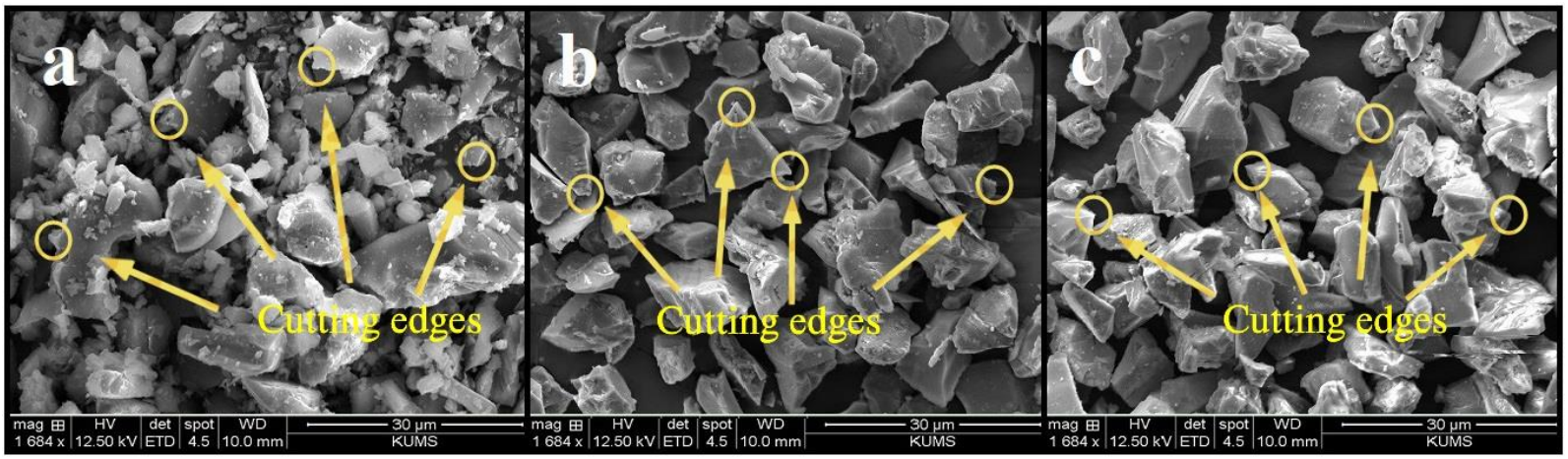

Fig 8. The SEM images of abrasive grain; [size: (a) 18μm, (b) 23 μm, (c) 28 (c)].

Table 4 Plan of experiments based on the Response Surface Method (RSM).

StdOrder	RunOrder	PtType	S (rpm)	W (mm)	A (μm)	Final Ra (nm)
15	1	0	450	1.5	23	178
3	2	1	300	2.0	18	258
9	3	-1	300	1.5	23	217
1	4	1	300	1.0	18	149
18	5	0	450	1.5	23	169
28	6	1	600	2.0	28	215
23	7	1	300	2.0	18	219
35	8	0	450	1.5	23	186
25	9	1	300	1.0	28	222
39	10	0	450	1.5	23	180
33	11	-1	450	1.5	18	216
38	12	0	450	1.5	23	172
5	13	1	300	1.0	28	210
34	14	-1	450	1.5	28	244
4	15	1	600	2.0	18	138
6	16	1	600	1.0	28	164
36	17	0	450	1.5	23	175
14	18	-1	450	1.5	28	262
10	19	-1	600	1.5	23	141
13	20	-1	450	1.5	18	180
26	21	1	600	1.0	28	170
29	22	-1	300	1.5	23	204
20	23	0	450	1.5	23	176
19	24	0	450	1.5	23	183
12	25	-1	450	2.0	23	206
17	26	0	450	1.5	23	173
2	27	1	600	1.0	18	46
31	28	-1	450	1.0	23	146
21	29	1	300	1.0	18	143
37	30	0	450	1.5	23	175
11	31	-1	450	1.0	23	132
40	32	0	450	1.5	23	172

8	33	1	600	2.0	28	199
27	34	1	300	2.0	28	289
32	35	-1	450	2.0	23	193
24	36	1	600	2.0	18	125
22	37	1	600	1.0	18	59
16	38	0	450	1.5	23	180
30	39	-1	600	1.5	23	130
7	40	1	300	2.0	28	294

5. Results and discussion

In this section, first, the effects of stirring-blades speed, working gap, and abrasive grain size on the surface rouhghness (Ra) obtained from experimental results were investigated. Then, the experimental and theoretical results were compared.

5.1 Effects of stirring-blades speed on Ra

Figure 9 plots the stirring-blades speed versus surface roughness. As can be seen, a rise in the stirring-blade speed reduces the change in the average surface roughness (ΔRa). The normal force ($\boldsymbol{F_n}$) is responsible for penetrating the workpiece, while the tangential force ($\boldsymbol{F_t}$) removes material from the workpiece. The removal of material increases as the stirring-blade speed ($\boldsymbol{v_s}$) rises. Also, an increase in the stirring-blade speed enhances the relative speed ($\boldsymbol{v_r}$) of the stirring-blade and the workpiece. Thus, the speed of the abrasive ($\boldsymbol{v_a}$) is equal to the relative speed of the stirring-blade and workpiece when meeting (i.e., $\boldsymbol{v_r = v_a = v_s + v_w}$). Moreover, based on Eq. (5), the $\boldsymbol{F_n}$ is directly related to the squared abrasive grain speed when meeting the workpiece. Therefore, an increase in the stirring-blade speed and abrasive grain speed raises the indentation force and indentation depth. Then, a rapid movement of the abrasive on the surface increases the shear stress of the workpiece surface. As the stirring-blade speed rises, a larger number of grains ($\boldsymbol{N_s}$) engage in the polishing process. The increased number of grains in polishing raises the collisions with the surface. Thus, according to Eqs. (23) and (22), the real contact area ($\boldsymbol{L_i}$) and traveled path length ($\boldsymbol{L_w}$) of abrasive grains increase. Furthermore, the increased number of grains in polishing raises the number of active grains ($\boldsymbol{N_a}$) on the roughness. Based on Eqs. (29) and (31), roughness removal rises as the number of active gains increases, enhancing the MRR, reducing surface roughness, and improving the quality of the surface. Roughness reduction was maximized at a stirring-blades speed of 600 rpm, a working gap of 1 mm, and abrasive grain size of 18 μm (from the initial Ra of 164 nm to the final Ra of 64 nm).

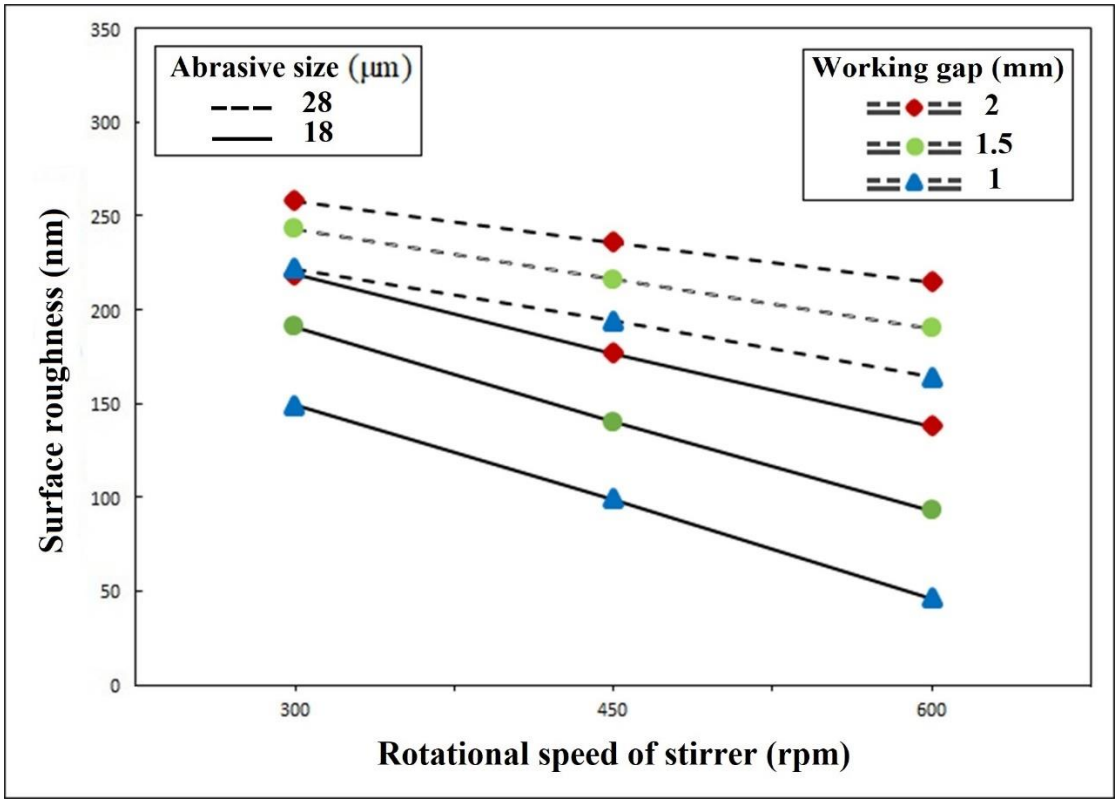

Fig. 9 Stirring-blades speed versus surface roughness.

5.2 Effects of working gap on Ra

Figure 10 plots surface roughness versus the working gap. As can be seen, a rise in the working gap raises the ΔRa. Increased working gap leads to the involvement of fewer abrasive grains in the finishing process since the abrasive grains need to travel a longer path to meet the workpiece surface (Fig. 1(b)). According to Eq. (31), the total number of abrasive grains ($\boldsymbol{N_t}$) is directly related to the squared stirrer radius. In other words, the working gap increases as the stirrer radius reduces, and this reduces the total number of abrasive grains engaging in the polishing process. Fewer cutting edges of abrasive grain meet the surface when the total number of grains decreases. As a result, $\boldsymbol{F_f}$ declines on the surface. This effect becomes stronger particularly when the relative speed between the stirrer and workpiece is lower since $\boldsymbol{F_n}$ is inversely related to $\bar{\boldsymbol{R}}$, according to Eq. (5). Thus, reduced $\boldsymbol{F_n}$ and $\boldsymbol{F_t}$ diminish the finishing force $\boldsymbol{F_f}$. The largest change in the average surface roughness was found to be 162 nm at a stirring-blade speed of 600 rpm, a working gap of 1.5 mm, and abrasive grain size of 23 μm.

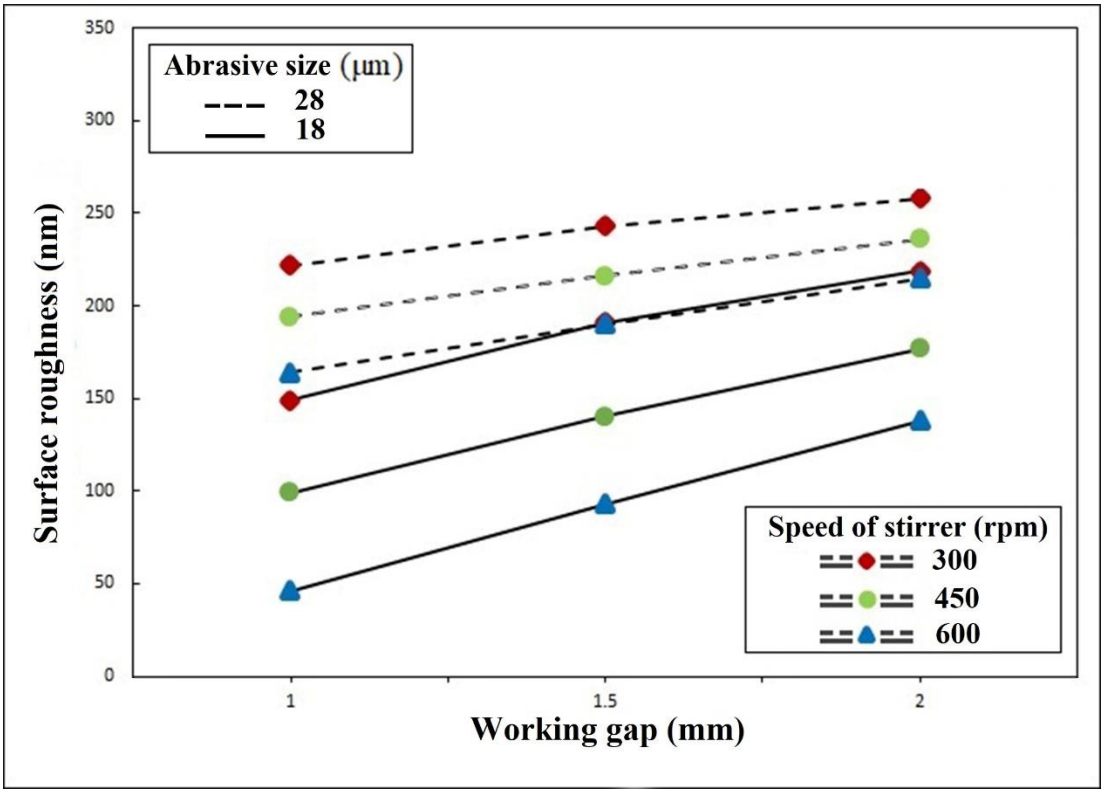

Fig. 10 Working gap versus surface roughness.

5.3 Effects of abrasive grain size on Ra

Figure 11 plots surface roughness versus the abrasive grain size before and after RAF. As can be seen, the MRR increases as the grain size rises since larger abrasive grains have stronger cutting edges to remove material. The finishing force $\boldsymbol{F_f}$ is responsible for finishing. According to Eq. (18), $\boldsymbol{F_n}$ and $\boldsymbol{F_t}$ are directly related to the abrasive grain size, and a rise in $\boldsymbol{F_n}$ and $\boldsymbol{F_t}$ increases $\boldsymbol{F_f}$. This reduces the roughness of the surface. However, each grain has a limited ability to remove roughness. Based on Eq. (34), the ultimate surface roughness is related to the squared abrasive grain size. Thus, the roughness of the surface cannot be significantly decreased using abrasive grains with a fixed size since the grains would not be able to remove smaller rough points above an optimal level. Thus, above the optimal level, not only does not surface roughness further decrease but also the quality of the surface may decline. To tackle this drawback, it is required to utilize abrasive grains with smaller sizes than the previous stage. The present study employed abrasive grains with sizes of 18, 23, and 28 μm. The increase in the abrasive grain size from 18 to 28 μm enhanced the ability of the grains to remove roughness. The larger abrasive grains (23 and 28 μm) had greater abilities than the 18-μm ones to remove roughness. The highest surface reduction was found to be 198.60 μm using the 23-μm grains. Figure 12 shows the unfinished and RAF-finished workpiece surfaces.

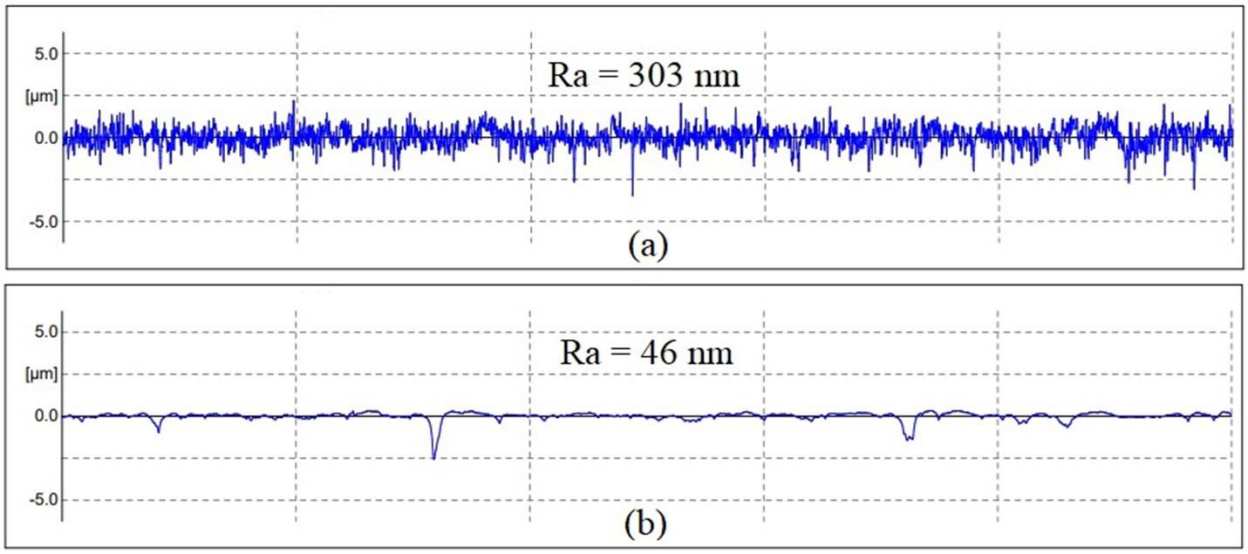

Fig. 11 Surface roughness plot; (a) before and (b) after process.

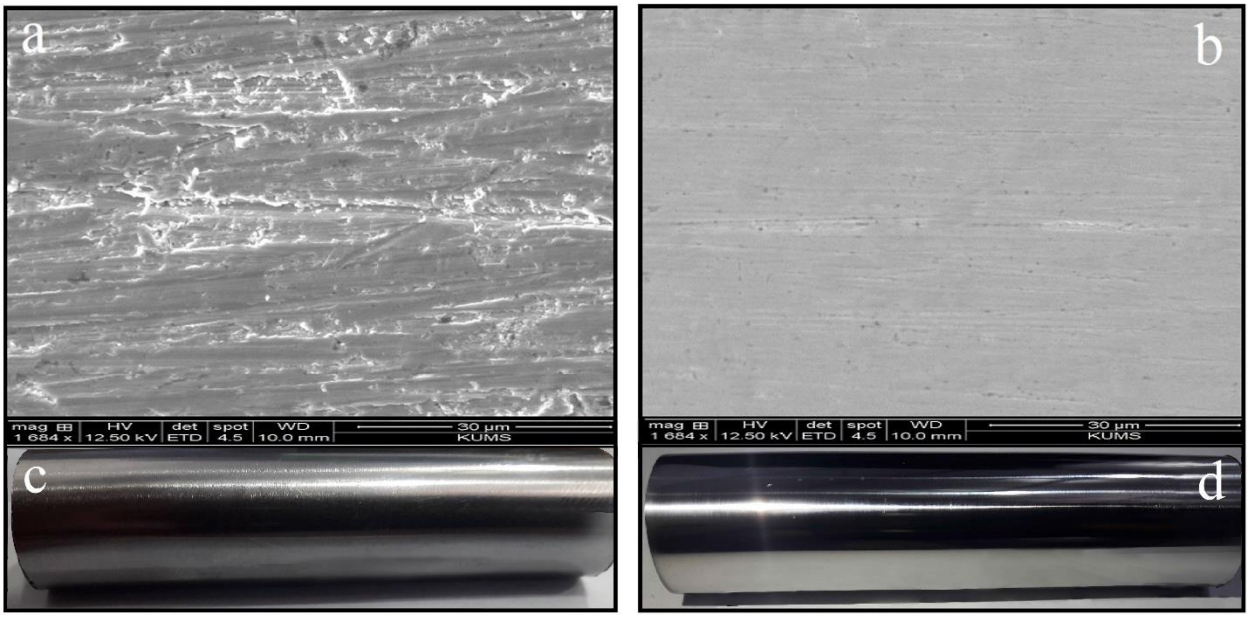

Fig. 12 SEM images and surfaces of workpiece; (a and c) before, and (b and d) after process.

5.4 Comparison of theoretical and experimental results

Figure 13 compares the theoretical and experimental material removal results. To asses the repeatability of the experiments and verify the experiment results, a palne of experiments were designed based on the RSM, as shown in the Table 4. According to this, the standard devation of the repeated experiments was measured, as shown in the Fig.13. As can be seen, the experimental material removal results were higher than the theoretical results. This can be attributed to the theoretical assumptions and the differences from real-life conditions. The theoretical investigation assumed the same shape (spherical) and size of abrasive grains for simplification purposes, whereas real-life grains have different shapes and sizes with a non-uniform distribution. This significantly affects the MRR and increases the removal of material in the experimental conditions.

Moreover, the theoretical investigation assumed each abrasive grain to have an active cutting edge, whereas real-life abrasive grains, may have several active cutting edges, as shown in Fig.8. This is an essential explanation for the difference between the theoretical and experimental material removals.

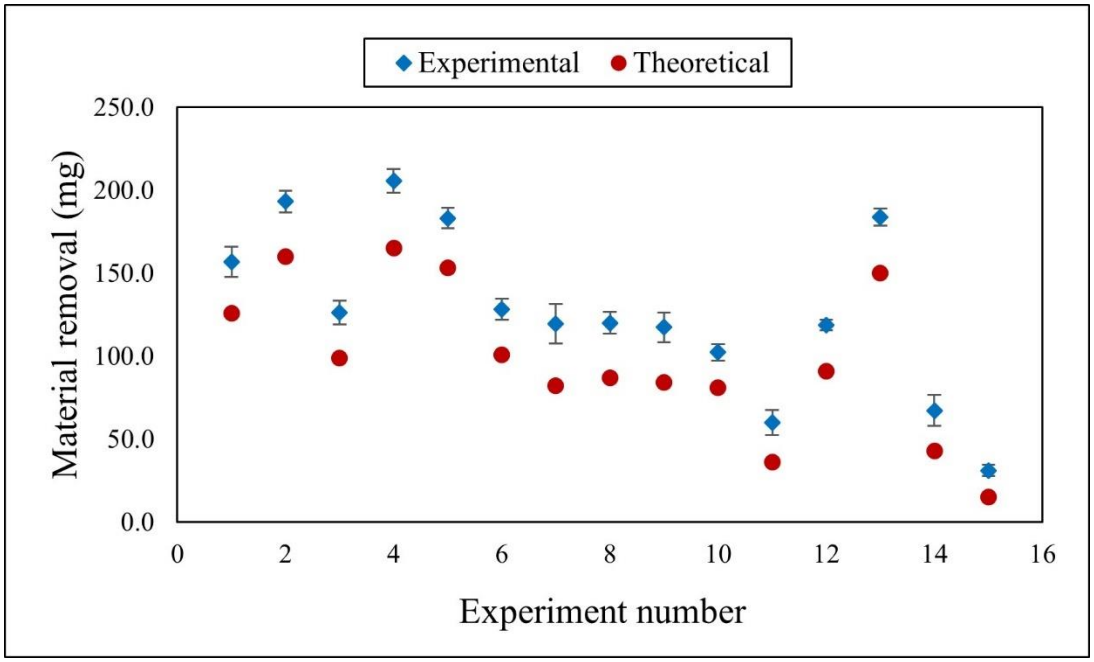

Fig. 13 Comparison of theoretical and experimental results of removed material.

Figure 14 compares the theoretical and experimental surface roughness results. The experimental roughness reductions were larger than the theoretical ones. The precent error between theoretical and experimental results can be obtained as follows [41]:

$$\boldsymbol{Precent\ error}\ (\%) = \frac{|\boldsymbol{Theoretical\ value} - \boldsymbol{Experimental\ value}|}{|\boldsymbol{Theoretical\ value}|} \times \mathbf{100} \qquad (\mathbf{36})$$

The experimental results were relatively in good agreement with the theoretical results so that the maximum error was 24%. The difference between theoretical and experimental results can be attributed to the theoretical assumptions. The theoretical investigation assumed a uniform roughness profile without a statistical distribution for the workpiece, while a real-life workpiece surface has a non-uniform distribution of roughness. Due to the non-uniform surface roughness profile, each abrasive grain shows unpredictable, random behavior when meeting the surface, leading to different experimental and theoretical roughness results. Overall, the theoretical assumptions can be claimed to be the most important explanation for the differences between the theoretical and experimental results.

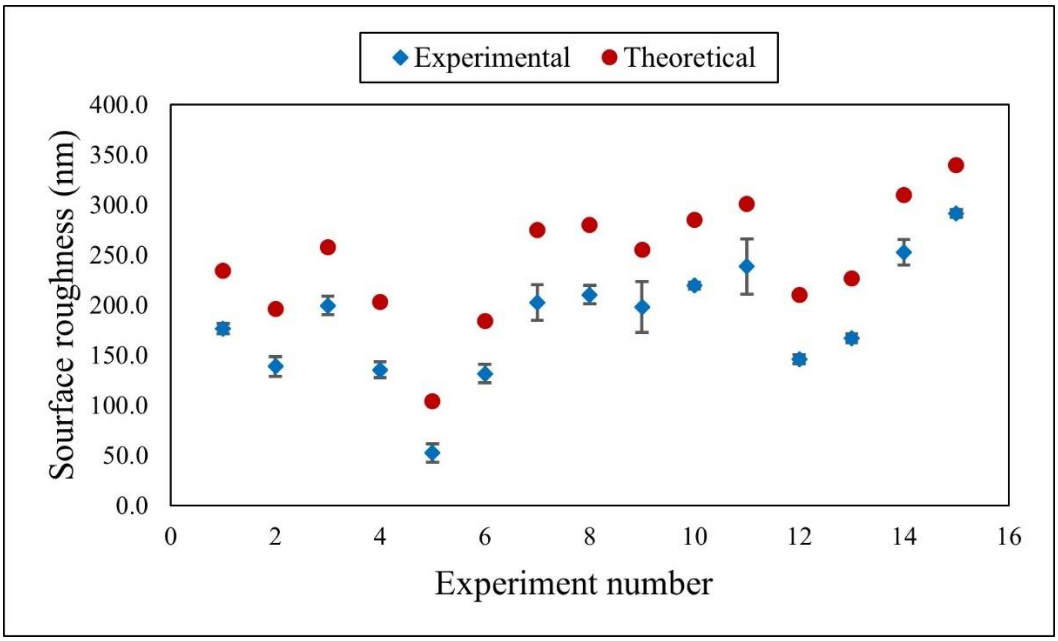

Fig. 14 Comparison of theoretical and experimental results of surface roughness (Ra).

6. Conclusion

The present study proposed a new theoretical model to predict surface roughness in the RAF process. A number of experiments were implemented on some process parameters to validate the proposed theoretical model. The findings can be summarized as:

1. A rise in the stirring-blades speed increased the number of active abrasive grains and raised F_n and F_t, reducing surface roughness. Surface roughness was minimized from 164 to 46 nm.
2. An increase in the working gap diminished the forces acting on the workpiece, reducing the ΔRa. The largest ΔRa was obtained to be 162 nm at a stirring-blade speed of 600 rpm, a working gap of 1.5 mm, and an abrasive grain size of 23 μm.
3. Larger abrasive grains have more cutting edges. This increases the ability of grains to remove material when meeting the workpiece surface, increasing MRR and reducing surface roughness. The largest material removal was found to be 198.60 mm using abrasive grains with a size of 23 μm.
4. The experimental results were relatively in good agreement with the theoretical results, so that the maximum error was about 24%.
5. It can be said that the differences between the theoretical and experimental results arose from the theoretical simplifying assumptions.

References

[1] F. Hashimoto *et al.*, "Abrasive fine-finishing technology," *CIRP Ann Manuf Technol*, vol. 65, no. 2, pp. 597–620, Jan. 2016, doi: 10.1016/j.cirp.2016.06.003.

[2] M. Rezayat, M. S. Yazdi, M. D. Zandi, and A. Azami, "Tribological and corrosion performance of electrodeposited Ni–Fe/Al2O3 coating," *Results in Surfaces and Interfaces*, vol. 9, p. 100083, Nov. 2022, doi: 10.1016/J.RSURFI.2022.100083.

[3] M. Kumar, A. Alok, V. Kumar, and M. Das, "Advanced abrasive-based nano-finishing processes: challenges, principles and recent applications," *https://doi.org/10.1080/10426914.2021.2001509*, vol. 37, no. 4, pp. 372–392, 2021, doi: 10.1080/10426914.2021.2001509.

[4] A. Azami, Z. Salahshournejad, E. Shakouri, A. R. Sharifi, and P. Saraeian, "Influence of nano-minimum quantity lubrication with MoS2 and CuO nanoparticles on cutting forces and surface roughness during grinding of AISI D2 steel," *J Manuf Process*, vol. 87, pp. 209–220, Feb. 2023, doi: 10.1016/J.JMAPRO.2023.01.029.

[5] R. K. Jain, V. K. Jain, and P. M. Dixit, "Modeling of material removal and surface roughness in abrasive flow machining process," *Int J Mach Tools Manuf*, vol. 39, no. 12, pp. 1903–1923, 1999, doi: 10.1016/S0890-6955(99)00038-3.

[6] V. K. Gorana, V. K. Jain, and G. K. Lal, "Forces prediction during material deformation in abrasive flow machining," *Wear*, vol. 260, no. 1–2, pp. 128–139, Jan. 2006, doi: 10.1016/j.wear.2004.12.038.

[7] V. K. Gorana, V. K. Jain, and G. K. Lal, "Prediction of surface roughness during abrasive flow machining," *International Journal of Advanced Manufacturing Technology*, vol. 31, no. 3–4, pp. 258–267, 2006, doi: 10.1007/s00170-005-0197-4.

[8] S. Singh, D. Kumar, and M. Ravi Sankar, "Experimental, Theoretical, and Simulation Comparative Study of Nano Surface Roughness Generated during Abrasive Flow Finishing Process," *Journal of Manufacturing Science and Engineering, Transactions of the ASME*, vol. 139, no. 6, pp. 1–12, 2017, doi: 10.1115/1.4035417.

[9] Y. Fu, H. Gao, Q. Yan, and X. Wang, "A new predictive method of the finished surface profile in abrasive flow machining process," *Precis Eng*, vol. 60, pp. 497–505, Nov. 2019, doi: 10.1016/j.precisioneng.2019.08.011.

[10] C. Bouland, V. Urlea, K. Beaubier, M. Samoilenko, and V. Brailovski, "Abrasive flow machining of laser powder bed-fused parts: Numerical modeling and experimental validation," *J Mater Process Technol*, vol. 273, p. 116262, Nov. 2019, doi: 10.1016/j.jmatprotec.2019.116262.

[11] M. R. Sankar, V. K. Jain, and J. Ramkumar, "Experimental investigations into rotating workpiece abrasive flow finishing," *Wear*, vol. 267, no. 1–4, pp. 43–51, Jun. 2009, doi: 10.1016/j.wear.2008.11.007.

[12] M. Ravi Sankar, V. K. Jain, and J. Ramkumar, "Rotational abrasive flow finishing (R-AFF) process and its effects on finished surface topography," *Int J Mach Tools Manuf*, vol. 50, no. 7, pp. 637–650, Jul. 2010, doi: 10.1016/j.ijmachtools.2010.03.007.

[13] S. Singh and H. S. Shan, "Development of magneto abrasive flow machining process," *Int J Mach Tools Manuf*, vol. 42, no. 8, pp. 953–959, Jun. 2002, doi: 10.1016/S0890-6955(02)00021-4.

[14] A. M. Wani, V. Yadava, and A. Khatri, "Simulation for the prediction of surface roughness in magnetic abrasive flow finishing (MAFF)," *J Mater Process Technol*, 2007, doi: 10.1016/j.jmatprotec.2007.02.036.

[15] G. Venkatesh, A. K. Sharma, and P. Kumar, "On ultrasonic assisted abrasive flow finishing of bevel gears," *Int J Mach Tools Manuf*, vol. 89, pp. 29–38, Feb. 2015, doi: 10.1016/j.ijmachtools.2014.10.014.

[16] A. Barman and M. Das, "Design and fabrication of a novel polishing tool for finishing freeform surfaces in magnetic field assisted finishing (MFAF) process," *Precis Eng*, vol. 49, pp. 61–68, Jul. 2017, doi: 10.1016/j.precisioneng.2017.01.010.

[17] A. Misra, P. M. Pandey, and U. S. Dixit, "Modeling of material removal in ultrasonic assisted magnetic abrasive finishing process," *Int J Mech Sci*, vol. 131–132, pp. 853–867, Oct. 2017, doi: 10.1016/j.ijmecsci.2017.07.023.

[18] C. W. Kum, T. Sato, J. Guo, K. Liu, and D. Butler, "A novel media properties-based material removal rate model for magnetic field-assisted finishing," *Int J Mech Sci*, vol. 141, pp. 189–197, Jun. 2018, doi: 10.1016/j.ijmecsci.2018.04.006.

[19] Y. Gao, Y. Zhao, G. Zhang, F. Yin, and H. Zhang, "Modeling of material removal in magnetic abrasive finishing process with spherical magnetic abrasive powder," *Int J Mech Sci*, vol. 177, p. 105601, Jul. 2020, doi: 10.1016/j.ijmecsci.2020.105601.

[20] J. Zhang, H. Wang, A. Senthil Kumar, and M. Jin, "Experimental and theoretical study of internal finishing by a novel magnetically driven polishing tool," *Int J Mach Tools Manuf*, vol. 153, p. 103552, Jun. 2020, doi: 10.1016/j.ijmachtools.2020.103552.

[21] S. Jha and V. K. Jain, "Design and development of the magnetorheological abrasive flow finishing (MRAFF) process," *Int J Mach Tools Manuf*, vol. 44, no. 10, pp. 1019–1029, Aug. 2004, doi: 10.1016/j.ijmachtools.2004.03.007.

[22] A. Sidpara and V. K. Jain, "Theoretical analysis of forces in magnetorheological fluid based finishing process," *Int J Mech Sci*, vol. 56, no. 1, pp. 50–59, 2012, doi: 10.1016/j.ijmecsci.2012.01.001.

[23] A. K. Singh, S. Jha, and P. M. Pandey, "Mechanism of material removal in ball end magnetorheological finishing process," *Wear*, vol. 302, no. 1–2, pp. 1180–1191, Apr. 2013, doi: 10.1016/j.wear.2012.11.082.

[24] Z. Alam and S. Jha, "Modeling of surface roughness in ball end magnetorheological finishing (BEMRF) process," *Wear*, vol. 374–375, pp. 54–62, Mar. 2017, doi: 10.1016/j.wear.2016.11.039.

[25] S. K. Paswan, T. S. Bedi, and A. K. Singh, "Modeling and simulation of surface roughness in magnetorheological fluid based honing process," *Wear*, vol. 376–377, pp. 1207–1221, Apr. 2017, doi: 10.1016/j.wear.2016.11.025.

[26] K. Arora and A. K. Singh, "Magnetorheological finishing of UHMWPE acetabular cup surface and its performance analysis," *Materials and Manufacturing Processes*, vol. 35, no. 14, pp. 1631–1649, Oct. 2020, doi: 10.1080/10426914.2020.1784928.

[27] G. Ghosh, A. Sidpara, and P. P. Bandyopadhyay, "Experimental and theoretical investigation into surface roughness and residual stress in magnetorheological finishing of OFHC copper," *J Mater Process Technol*, vol. 288, p. 116899, Feb. 2021, doi: 10.1016/j.jmatprotec.2020.116899.

[28] Y. Cao, J. Yin, W. Ding, and J. Xu, "Alumina abrasive wheel wear in ultrasonic vibration-assisted creep-feed grinding of Inconel 718 nickel-based superalloy," *J Mater Process Technol*, vol. 297, p. 117241, Nov. 2021, doi: 10.1016/J.JMATPROTEC.2021.117241.

[29] Q. Miao *et al.*, "Creep feed grinding induced gradient microstructures in the superficial layer of turbine blade root of single crystal nickel-based superalloy," *International Journal of Extreme Manufacturing*, vol. 3, no. 4, p. 045102, Aug. 2021, doi: 10.1088/2631-7990/AC1E05.

[30] Y. CAO, Y. ZHU, W. DING, Y. QIU, L. WANG, and J. XU, "Vibration coupling effects and machining behavior of ultrasonic vibration plate device for creep-feed grinding of Inconel 718 nickel-based superalloy," *Chinese Journal of Aeronautics*, vol. 35, no. 2, pp. 332–345, Feb. 2022, doi: 10.1016/J.CJA.2020.12.039.

[31] Y. Cao, W. Ding, B. Zhao, X. Wen, S. Li, and J. Wang, "Effect of intermittent cutting behavior on the ultrasonic vibration-assisted grinding performance of Inconel718 nickel-based superalloy," *Precis Eng*, vol. 78, pp. 248–260, Nov. 2022, doi: 10.1016/J.PRECISIONENG.2022.08.006.

[32] Y. Cao *et al.*, "Development and performance of a novel ultrasonic vibration plate sonotrode for grinding," *J Manuf Process*, vol. 57, pp. 174–186, Sep. 2020, doi: 10.1016/J.JMAPRO.2020.06.030.

[33] A. Azami and A. Azizi, "Rotational abrasive finishing (RAF); novel design for micro/nanofinishing," *International Journal of Advanced Manufacturing Technology*, vol. 91, no. 9–12, pp. 3159–3167, Aug. 2017, doi: 10.1007/s00170-017-0016-8.

[34] A. A. Gilan and A. Azizi, "Rotational abrasive micro/nano-finishing." Google Patents, Feb. 12, 2019.

[35] A. A. Gilan, A. Azizi, and A. Khoshanjam, "Rotational abrasive micro/nano-finishing." Google Patents, May 31, 2022.

[36] V. K. Jain, R. Kumar, P. M. Dixit, and A. Sidpara, "Investigations into abrasive flow finishing of complex workpieces using FEM," *Wear*, vol. 267, no. 1–4, pp. 71–80, Jun. 2009, doi: 10.1016/J.WEAR.2008.11.005.

[37] A. Azami, A. Azizi, A. Khoshanjam, and M. Hadad, "A new approach for nanofinishing of complicated-surfaces using rotational abrasive finishing process," *Materials and Manufacturing Processes*, vol. 35, no. 8, pp. 940–950, Jun. 2020, doi: 10.1080/10426914.2020.1750631.

[38] A. F. Alajmi, B. P. Hu, and M. Ramulu, "Experimental solid particle erosion of silicon nitride: Optical investigation," *Ceram Int*, vol. 47, no. 2, pp. 2743–2750, Jan. 2021, doi: 10.1016/j.ceramint.2020.09.127.

[39] D. I. N. E. N. ISO 4288, "'Geometrical Product Specifications (GPS)-Surface texture: Profile method-Rules and procedures for the assessment of surface texture.'" 1996.

[40] C. Prakash *et al.*, "Experimental investigation into nano-finishing of β-TNTZ alloy using magnetorheological fluid magnetic abrasive finishing process for orthopedic applications," *Journal of Materials Research and Technology*, vol. 11, pp. 600–617, Mar. 2021, doi: 10.1016/J.JMRT.2021.01.046.

[41] Z. Alam, D. A. Khan, F. Iqbal, and S. Jha, "Theoretical and Experimental Study on Forces in Ball End Magnetorheological Finishing Process," *Lecture Notes in Mechanical Engineering*, pp. 391–401, 2023, doi: 10.1007/978-981-19-3866-5_33/FIGURES/6.

Highlights

- A new theoretical model for surface roughness prediction in the rotational abrasive finishing (RAF) process was proposed.
- To validate the new proposed theoretical model, a number of influential parameters were empirically investigated.
- The theoretical results were relatively in good agreement with the experimental results.
- The assumptions of the theoretical model can be claimed to be the most important explanation for the difference between the theoretical and experimental results.

Author Agreement Statement

We the undersigned declare that this manuscript is original, has not been published before, and is not currently being considered for publication elsewhere.

We confirm that the manuscript has been read and approved by all named authors and that there are no other persons who satisfied the criteria for authorship but are not listed. We further confirm that the order of authors listed in the manuscript has been approved by all of us.

We understand that the Corresponding Author is the sole contact for the Editorial process. He/she is responsible for communicating with the other authors about progress, submissions of revisions, and final approval of proofs Signed by all authors as follows:

Aref Azami, Ali Khoshanjam, Ramon Jerez-Mesa, Jordi Lluma-Fuentes, Jose Antonito Travieso-Rodriguez,

Declaration of interests

☒ The authors declare that they have no known competing financial interests or personal relationships that could have appeared to influence the work reported in this paper.

☐ The authors declare the following financial interests/personal relationships which may be considered as potential competing interests: